

Article

Soot Oxidation in a Plasma-Catalytic Reactor: A Case Study of Zeolite-Supported Vanadium Catalysts

Xinbo Zhu ^{1,*}, Hanpeng Wu ¹, Jianbin Luo ¹, Jin Liu ¹, Jiahao Yan ¹, Zijian Zhou ^{2,*}, Zhengda Yang ³, Ye Jiang ³, Geng Chen ¹ and Guohua Yang ¹

¹ Faculty of Maritime and Transportation, Ningbo University, Ningbo 315211, China; wuhanpeng1203@163.com (H.W.); ljb15667840050a@163.com (J.L.); a853800339@126.com (J.L.); yanjiahao0623@163.com (J.Y.); chengeng@nbu.edu.cn (G.C.); yangguohua@nbu.edu.cn (G.Y.)

² State Key Laboratory of Coal Combustion, Huazhong University of Science and Technology, Wuhan 430074, China

³ College of New Energy, China University of Petroleum (East China), 66 West Changjiang Road, Qingdao 266580, China; yzd019@upc.edu.cn (Z.Y.); jiangye@upc.edu.cn (Y.J.)

* Correspondence: zhuxinbo@nbu.edu.cn (X.Z.); zhouzj2012@hust.edu.cn (Z.Z.)

Abstract: The plasma-catalytic oxidation of soot was studied over zeolite-supported vanadium catalysts, while four types of zeolites (MCM-41, mordenite, USY and 5A) were used as catalyst supports. The soot oxidation rate followed the order of V/MCM-41 > V/mordenite > V/USY > V/5A, while 100% soot oxidation was achieved at 54th min of reaction over V/MCM-41 and V/mordenite. The CO₂ selectivity of the process follows the opposite order of oxidation rate over the V/M catalyst. A wide range of catalyst characterizations including N₂ adsorption–desorption, XRD, XPS, H₂-TPR and O₂-TPD were performed to obtain insights regarding the reaction mechanisms of soot oxidation in plasma-catalytic systems. The redox properties were recognized to be crucial for the soot oxidation process. The effects of discharge power, gas flow rate and reaction temperature on soot oxidation were also investigated. The results showed that higher discharge power, higher gas flow rate and lower reaction temperature were beneficial for soot oxidation rate. However, these factors would impose a negative effect on CO₂ selectivity. The proposed “plasma-catalysis” method possessed the unique advantages of quick response, mild operation conditions and system compactness. The method could be potentially applied for the regeneration of diesel particulate filters (DPF) at low temperatures and contribute to the the emission control of diesel engines.

Keywords: plasma; catalysis; soot oxidation; zeolite; vanadium



Citation: Zhu, X.; Wu, H.; Luo, J.; Liu, J.; Yan, J.; Zhou, Z.; Yang, Z.; Jiang, Y.; Chen, G.; Yang, G. Soot Oxidation in a Plasma-Catalytic Reactor: A Case Study of Zeolite-Supported Vanadium Catalysts. *Catalysts* **2022**, *12*, 677. <https://doi.org/10.3390/catal12070677>

Academic Editors: Boxiong Shen and Peng Yuan

Received: 28 April 2022

Accepted: 13 June 2022

Published: 21 June 2022

Publisher's Note: MDPI stays neutral with regard to jurisdictional claims in published maps and institutional affiliations.



Copyright: © 2022 by the authors. Licensee MDPI, Basel, Switzerland. This article is an open access article distributed under the terms and conditions of the Creative Commons Attribution (CC BY) license (<https://creativecommons.org/licenses/by/4.0/>).

1. Introduction

The diesel engine has been widely used in marine transportation and industries due to its strong power, good fuel economy and high reliability. However, soot emission from diesel engines has become one of the major sources of air pollution in recent years [1]. Great efforts have been devoted to the development of soot emission control technologies. Recently, the combination of a heterogeneous catalyst and a diesel particulate filter, also known as a catalytic diesel particulate filter (CDPF), has been recognized as a promising technology for soot emission control because the presence of catalysts could contribute to a decrease of the ignition temperature of soot and maintain the low back pressure of the CDPF for a long time [2,3].

The key point for CDPF technology was the development of high-efficiency catalysts for soot oxidation. Currently, the research on catalysts for soot oxidation mainly focuses on noble metals, transition metal oxides, perovskite catalysts and spinel catalysts [4,5]. Researchers reported that the ignition temperature of soot could be reduced to 400~450 °C in the presence of heterogeneous catalysts, which is still much higher than the effluent temperature of a diesel engine, especially during the start-up stage and normal operation

of marine diesel engine (below 200–300 °C) [3,6,7]. As a result, a solution enabling soot oxidation at a relatively low temperature is urgently needed.

More recently, the combination of non-thermal plasma and heterogeneous catalysts has become an emerging alternative for the oxidation of volatile organic compounds (VOCs) and the partial oxidation of hydrocarbons under atmospheric pressure and temperatures ranging from room temperature to 300 °C [8–10]. As with soot oxidation, Lu et al. reported that the oxidation of graphitic carbon over an Au/ γ -Al₂O₃ catalyst in a plasma environment was improved compared to pure γ -Al₂O₃ in the temperature range of 20 °C to 300 °C [11]. Liu et al. investigated plasma-catalytic oxidation of soot over a series of Ag and Co co-doped perovskite catalysts, while a soot oxidation rate of 85% was achieved at 200 °C over an La_{0.5}A_{0.5}Mn_{0.8}Co_{0.2}O₃ (A = Ag or Co) catalyst [12]. Although many kinds of catalysts have been incorporated for plasma-catalytic oxidation of soot, the use of a noble metal based catalyst composition may result in economic inefficiency and limit the potential industrial application of plasma-catalytic technology.

In addition to the active metal, the choice of catalyst support could significantly affect the performance of the plasma-catalytic system [13,14]. Patil et al. investigated the performance of plasma-catalytic NO_x synthesis over a wide range of catalyst supports, including α -Al₂O₃, γ -Al₂O₃, TiO₂, MgO, BaTiO₃ and quartz wool [15]. The presence of quartz wool and γ -Al₂O₃ in the plasma reactor doubled the NO_x production compared to using plasma alone, while the use of BaTiO₃ decreased the plasma-induced NO_x production. Kim et al. studied the effect of the Si/Al ratio of HY zeolites on 200 ppm benzene oxidation under plasma [16]. The results showed that the benzene oxidation rate decreases with an increase of the Si/Al ratio from 2.6 to 40, while the discharge region was also significantly reduced, as obtained by ICCD camera. Xie et al. compared the effect of Al₂O₃, L-MgO and H-MgO on NH₃ yield in a dielectric barrier discharge (DBD) reactor [17]. The results showed that the presence of H-MgO could slightly improve the NH₃ yield by 4% to 9.5% in the temperature range between 140 °C to 260 °C. To the best of our knowledge, most previous work mainly focused on the effect of support composition on the performance of soot oxidation, the mechanisms of how the physical structure of the support would affect the plasma-catalytic system, especially in the process of soot oxidation, were far from clearly understood [18,19].

In this work, vanadium was used as the active metal phase because it is currently widely used in commercial catalysts for diesel engine after-treatment. A series of zeolites—MCM-41, mordenite, USY and 5A—were used as supports for the V/M catalysts. The effects of different supports of V/M catalysts on the plasma-catalytic oxidation of soot was investigated in terms of the oxidation rate and CO₂ selectivity of the process. The roles of the V/M catalysts were evaluated by a series of catalyst characterizations of N₂ adsorption–desorption, X-ray diffraction (XRD), X-ray photoelectron spectroscopy (XPS), temperature-programmed reduction with H₂ (H₂-TPR) and temperature-programmed desorption of O₂ (O₂-TPD). The effects of various working conditions on the performance of plasma-catalytic soot oxidation were also discussed.

2. Results and Discussion

2.1. Textural Properties

Table 1 shows the physicochemical properties of the V/M catalysts. The S_{BET} and pore volumes of supported vanadium catalysts are significantly affected by the zeolite type because the values of USY-, mordenite- and MCM-41-supported catalysts are significantly higher than those of the 5A zeolite-supported catalysts. The highest S_{BET} and pore volumes are obtained over the V/MCM-41 catalyst, followed by V/USY, V/mordenite and V/5A, which is the same order as the zeolite support. Compared with the as-received zeolites (shown in Table S1), the specific surface area (S_{BET}) and pore volumes of the V/M catalysts slightly decreased. Taking the V/5A catalyst as an example, its S_{BET} and pore volume are 354 m²·g⁻¹ and 0.33 cm³·g⁻¹, respectively, while the S_{BET} and pore volume values for the support (5A zeolite) are 383 m²·g⁻¹ and 0.34 cm³·g⁻¹, respectively. The decrease

in S_{BET} and pore volume could be ascribed to the coverage of zeolite surfaces or partial blockage of the pore systems by vanadium species [20]. Similarly, the increase of average pore diameters for all vanadium-doped catalysts could be ascribed to the clogging of micropores while the meso- and macro-pores still exist. After doping with vanadium species, the zeolite support maintained its parent structure, while small particles of vanadium oxides would disperse on the surfaces of the V/M catalysts (shown in Figure S1). Similar results were observed in our previous work using $\text{MO}_x/\gamma\text{-Al}_2\text{O}_3$ catalysts for acetone oxidation in a plasma reactor [21].

Table 1. Physicochemical parameters of the V/M catalysts.

Catalyst	Specific Surface Area ($\text{m}^2\cdot\text{g}^{-1}$)	Pore Volume ($\text{cm}^3\cdot\text{g}^{-1}$)	Pore Diameter (nm)	$\text{V}^{4+}/(\text{V}^{4+} + \text{V}^{5+})$ (%)	$\text{O}_{\text{ads}}/(\text{O}_{\text{ads}} + \text{O}_{\text{latt}})$ (%)	H_2 Consumption ($\text{mmol}\cdot\text{g}^{-1}$)	O_2 Uptake ($\mu\text{mol}\cdot\text{g}^{-1}$)
V/MCM-41	817	0.74	3.6	47.4	59.8	0.112	0.332
V/mordenite	383	0.24	2.5	45.8	57.2	0.109	0.327
V/USY	670	0.43	2.6	37.2	56.5	0.122	0.239
V/5A	354	0.33	3.7	33.7	54.6	0.118	0.169

Figure 1 exhibits the XRD patterns of all the V/M catalysts. All XRD patterns show the typical diffraction peaks of their supports (as given in Figure S2). For the 5A zeolite-supported catalysts, the major diffraction peaks centered at the 2θ of 21.8° (3 0 0), 27.2° (3 2 1) and 24.1° (3 1 1) correspond to the cubic structure of A-type zeolites (JCPDS No.11-0589) [22]. As with V/USY and V/mordenite catalysts, their diffraction peaks are in accordance with the corresponding pristine zeolite structures (JCPDS PDF No.39-1380 and PDF No. 11-0155, respectively) [23,24]. For V/MCM-41, only a broad diffraction peak at 2θ of 22.0° is observed, which is correlated to amorphous SiO_2 (JCPDS PDF No. 29-0085) [25]. In addition, no distinct diffraction peaks of vanadium species are observed in the presented XRD patterns, indicating that the vanadium species may be in an amorphous state or highly dispersed on the zeolite surfaces. The peak intensities of the V/M catalysts are similar, indicating the differences in crystalline sizes are very small, except for V/MCM-41 (also shown in Table 1).

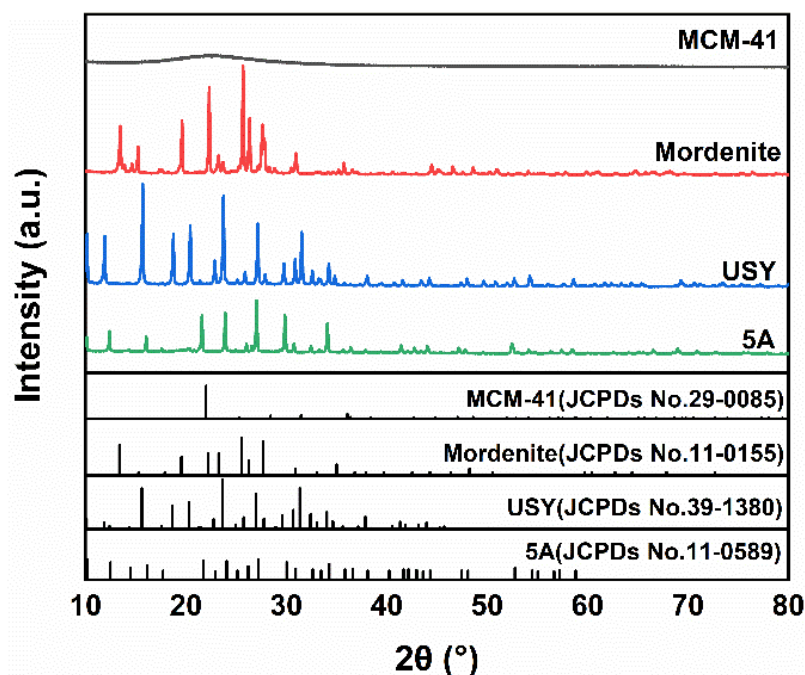


Figure 1. XRD patterns of the V/M (M = MCM-41, mordenite, USY and 5A) catalysts.

2.2. Redox Properties

XPS analysis was performed to obtain insights regarding the chemical states of the elements in the catalysts. Figure 2a shows the XPS spectra of V 2p for the V/M (M = MCM-41, mordenite, USY and 5A) catalysts. For all samples, two major peaks around 524 eV and 517 eV are observed in the XPS spectra of V 2p, which belong to V 2p_{1/2} and V 2p_{3/2}, respectively [20]. The deconvolution of the V 2p_{3/2} for the V/M catalysts exhibits two peaks centered at 517.4 eV and 516.4 eV. The former peak could be ascribed to the V⁵⁺ species, while the latter one belongs to the V⁴⁺ species. The relative content of V⁴⁺ species on the surfaces of V/M catalysts, defined as V⁴⁺/(V⁴⁺ + V⁵⁺), follows the order of V/MCM-41 (47.4%) > V/mordenite (45.8%) > V/USY (37.2%) > V/5A (33.7%).

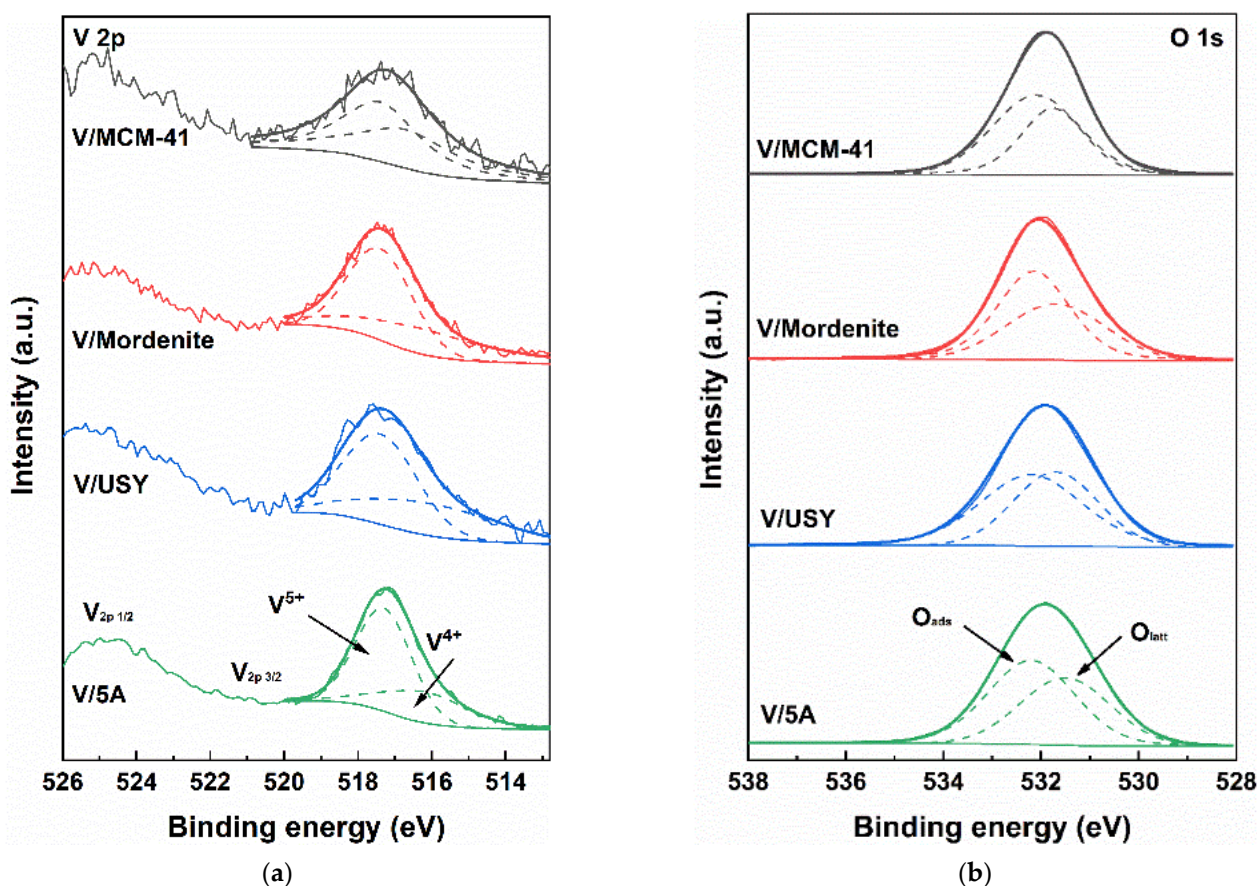


Figure 2. XPS spectra of the V/M (M = MCM-41, mordenite, USY and 5A) catalysts: (a) V 2p, (b) O 1s.

Figure 2b presents the XPS spectra of O 1s for all three V/M catalysts. The peaks located around 529.6–530.0 eV can be ascribed to the presence of lattice oxygen species (denoted as O_{latt}), while the peaks located between 531.4 eV and 532.1 eV could be ascribed to the existence of surface-adsorbed oxygen (denoted as O_{ads}) [26]. The relative content of O_{ads} for each V/M catalyst, defined as O_{ads}/(O_{ads} + O_{latt}), was calculated based on the XPS spectra (Table 1). The values of O_{ads}/(O_{ads} + O_{latt}) of all three catalysts vary from 54.6% to 59.8%, while the V/MCM-41 catalyst possesses the highest relative content of O_{ads}/(O_{ads} + O_{latt}). The values of O_{ads}/(O_{ads} + O_{latt}) of all zeolite supports are given in Table S1. Doping with vanadium oxide slightly improves the relative concentration of O_{ads} on the surface of V/M catalysts by ~1.7% compared with the bare zeolite supports. The O₂ uptake amount is also in the same order as the O_{ads}/(O_{ads} + O_{latt}) value (as presented in Table 1). The relative concentration of O_{ads} is closely correlated with the performance of soot oxidation, as the O_{ads} species is of better mobility compared with the O_{latt} species and could be easily activated to participate in the soot oxidation reaction on catalyst surfaces [27].

The reducibility of each V/M catalyst is tested using the H₂-TPR experiment as shown in Figure 3. For all V/M catalysts, broad reduction peaks between 400 °C and 550 °C could be observed, which could be attributed to the reduction of V⁵⁺ to V³⁺ species, as reported in previous work [20]. It is worth noting that the maximum reduction peak location shifted to a higher location from 480 °C (V/MCM-41) to 501 °C (V/mordenite), 504 °C (V/USY) and 528 °C (V/5A), respectively, indicating stronger interactions between vanadium species and the zeolite supports. The H₂ consumption amount was calculated based on the H₂-TPR profiles (Table 1). Among all tested catalysts, the highest H₂ consumption amount of 0.122 mmol·g⁻¹ was obtained over the V/MCM-41 catalyst, followed by the V/mordenite (0.118 mmol·g⁻¹), V/USY (0.112 mmol·g⁻¹) and V/5A (0.109 mmol·g⁻¹) catalysts. The similar H₂ consumption amounts may be attributed to the same theoretical amount of vanadium loading on the zeolites. However, it could be deduced that V/MCM-41 catalyst possesses better redox properties due to its abundant surface oxygen species (O_{ads}) and higher mobility compared to the other three catalysts, which are favorable properties for soot oxidation [28].

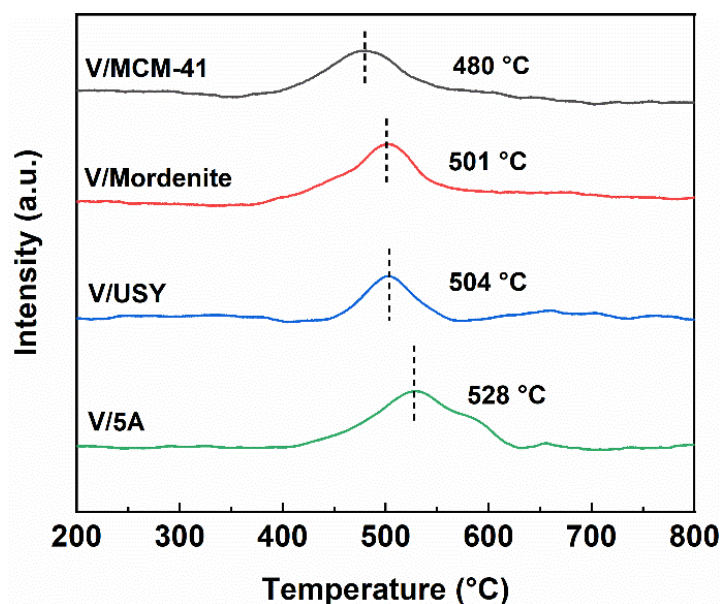


Figure 3. H₂-TPR profiles of the V/M (M = MCM-41, mordenite, USY and 5A) catalysts.

2.3. Effect of Catalyst Support on Plasma-Catalytic Soot Oxidation

Figure 4 shows the effects of the V/M catalysts on plasma-catalytic soot oxidation at a discharge power of 20 W as a function of time. It can be clearly seen that the soot oxidation rate increases steadily as the reaction goes on in the plasma reactor regardless of the type of zeolite support. During the 60-min reaction process, the soot oxidation rates are in order of V/MCM-41 > V/mordenite > V/USY > V/5A. For example, the soot oxidation rates over V/MCM-41, V/mordenite, V/USY and V/5A at 30th min are 78.6%, 66.4%, 55.2% and 50.5%, respectively. By the end of the 60-min reaction, all initially packed soot particles are oxidized to CO and CO₂ in the V/MCM-41- and V/mordenite-packed reactor, while the soot oxidation rates in the V/USY- and V/5A-packed plasma reactor are only 83.7% and 80.5%, respectively. The CO₂ selectivity values of the plasma-catalytic soot oxidation process over various V/M catalysts are compared using the data at 10th, 30th and 50th minute of the reaction (in Figure 4b). With the progress of soot oxidation, the CO₂ selectivity increases by only 1–2% during the reaction for all tested V/M catalysts. In addition, the order of CO₂ selectivity follows the opposite order of soot oxidation, namely: V/MCM-41 < V/mordenite < V/USY < V/5A.

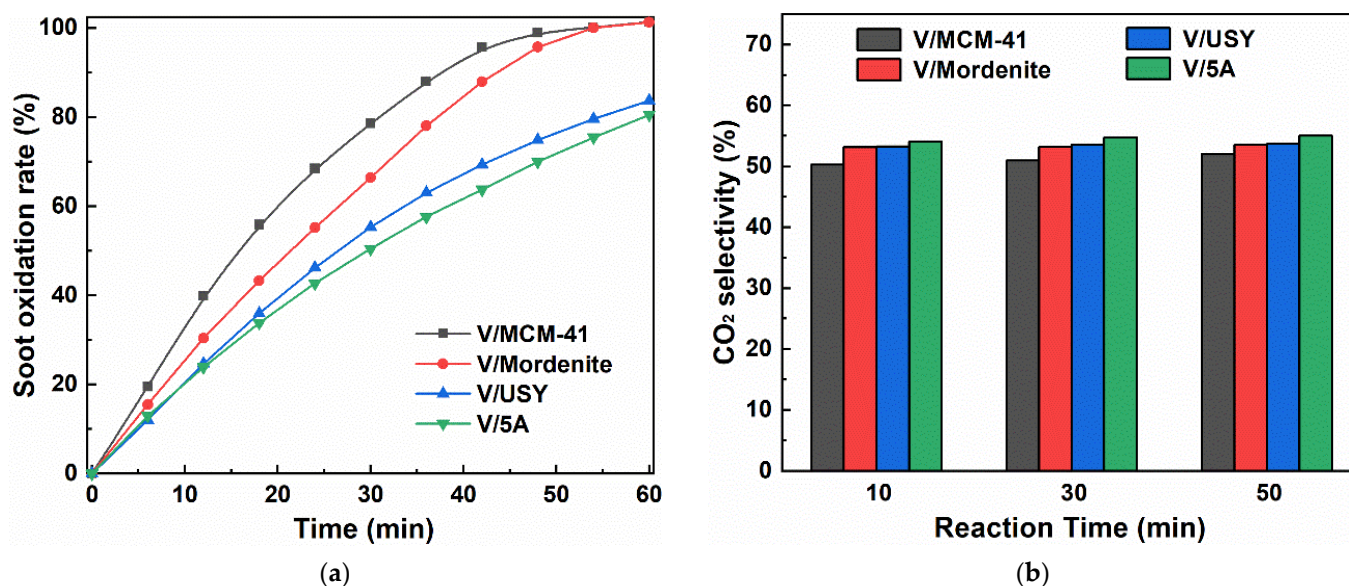


Figure 4. Plasma-catalytic oxidation of soot over V/M (M = MCM-41, mordenite, USY and 5A) catalysts at the discharge power: (a) oxidation rate and (b) CO₂ selectivity (Discharge power: 20 W, gas flow rate: 500 mL·min⁻¹ and reaction temperature: 25 °C).

In the plasma region, the energy dissipated into the reactor is utilized to generate energetic electrons and chemically reactive species for soot oxidation [29]. Early studies by Nagle et al. reported that there existed both active sites (S_{act}) and inactive sites (S_{inact}) on the surface of soot particles [30]. The inactive sites could be converted into active sites at high temperature or under the treatment of chemically reactive species. The active sites tended to react with oxidative species in the gas phase and form surface-adsorbed -CO groups. These groups would be further desorbed and form the final product of CO, while the CO could be further converted into CO₂ in the gas phase. It is worth noting that the formation on CO₂ on the surface of soot is likely to occur but is not the predominant process, as the activation energy of CO₂ formation on soot's surface is 3.6 times higher than that of CO formation [31]. It is widely recognized that NO₂ could be generated in a typical N₂/O₂ plasma. The presence of NO₂ in the plasma region would also facilitate the process of soot oxidation due to the strong oxidation capacity of NO₂. The plasma-generated NO₂ molecules could be transported onto soot for surface reactions. It can be inferred that the NO₂ would react directly with the elemental carbon in soot to form -C(NO₂) groups, and those groups would be further decomposed into -CO groups on the soot surfaces to form CO₂. In addition, NO₂ could be used to generate reactive oxygen species on catalyst surfaces, and these species would also participate in soot oxidation [32]. As a result, the soot particles packed into the DBD reactor could be oxidized by O· radicals, O₃ and NO₂ in the gas phase via the following reactions (Equations (1)–(7)):

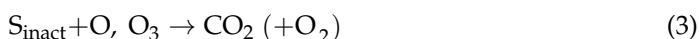


Figure 5 shows the Lissajous figures of the V/M catalyst-packed plasma reactor at a constant discharge power of 20 W. It can be seen from Figure 5 that the discharge characteristics are slightly changed by the presence of various V/M catalysts with different zeolite supports, as the shapes of the Lissajous figures shift slightly. It is well known that in a packed-bed DBD reactor, the discharge mode is the combination of surface discharge and weak filamentary micro-discharge, which propagates along the external and internal surfaces of the catalyst layer [33,34]. Moreover, the local electric field could be enhanced due to the presence of soot particles and catalyst pellets, which would be beneficial for the soot oxidation process. The dielectric constant of the catalyst would affect the current of plasma, as confirmed in our previous work [33]. It is interesting to note that due to the similar composition of the V/M catalysts in this work, the electrical characteristics of the plasma are not significantly affected by the presence of V/M catalysts.

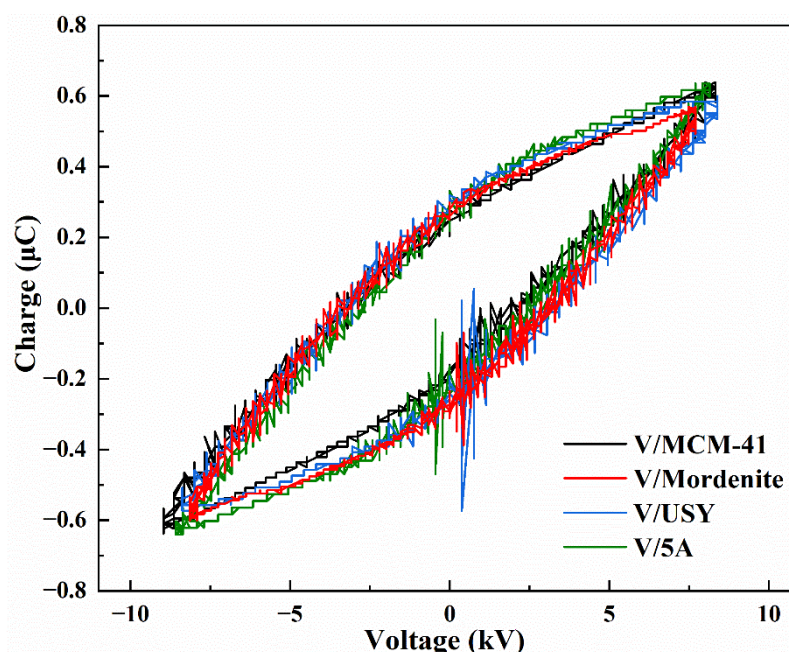


Figure 5. Lissajous figures for V/M catalyst-packed DBD reactors (Discharge power: 20 W, gas flow rate: $500 \text{ mL} \cdot \text{min}^{-1}$ and reaction temperature: $25 \text{ }^\circ\text{C}$).

Since the discharge characteristics for all four V/M catalyst-packed DBD reactors are quite similar, it can be deduced that the physicochemical properties of V/M catalysts would play a significant role in plasma-catalytic soot oxidation in this work. A V/M catalyst with a higher S_{BET} value would provide more adsorption and active sites for the heterogeneous catalytic reactions [35]. As the average diameter of soot in this work is much larger than the pore diameters of V/M catalysts, the active sites on the external surfaces of the V/M catalysts would be of great significance in soot oxidation. As shown in Figure 3, the presence of V^{4+} species indicated the formation of more surface oxygen vacancies on the V/M catalyst, considering the different ion radii of V^{5+} and V^{4+} species, as the electroneutrality at the interfaces of vanadium species and zeolites should be maintained. The relative concentration of $\text{V}^{4+}/(\text{V}^{4+} + \text{V}^{5+})$ of the V/MCM-41 catalyst is much higher than those of other three V/M catalysts. The abundant oxygen vacancies on the V/MCM-41 catalyst could serve as reservoirs of surface-adsorbed oxygen species and $\text{O} \cdot$ radicals in the gas phase for soot oxidation. It is well accepted that O_{ads} is highly reactive in oxidation reactions due to its better mobility compared to O_{latt} [36]. A catalyst with higher O_{ads} content could show better performance in soot oxidation because the released O_{ads} species would contribute to soot oxidation via the contact points between the V/M catalyst and soot particles. In addition, in the presence of catalysts, the released O_{ads} species would follow the same reaction pathways discussed above to form the final products of CO and CO_2 ,

while the enhancement of CO₂ selectivity seems to be necessary in future work. The H₂-TPR profiles also confirmed that the V/MCM-41 catalyst had the best reducibility compared to the other tested samples, while the lower reduction temperature of the V/MCM-41 catalyst indicated that the oxygen species on its surface were much easier to activate during the catalytic reaction. The consumed O_{ads} species would be replenished by plasma-generated O· radicals, O₃, etc. [37]. The O₂ uptake was also closely correlated with the abundant O_{ads} species on the surfaces of the V/M catalysts. The complete soot oxidation strongly depends on the oxygen adsorption capacity of the supported vanadium oxide catalysts and the facilitated oxygen transfer from catalyst surfaces to soot particles. It is worthy to note that the order of O₂ uptake below 300 °C was in accordance with H₂-TPR as shown in Table 1. A very good correlation between the oxidation rate and the redox properties of V/M catalysts could be observed in this work.

The energy efficiency of the plasma-catalytic soot oxidation process (calculated using Equations (S1) and (S2)) was used to make a comparison of the present work with the previously reported research on plasma-assisted soot oxidation. In this work, the energy efficiency of plasma-catalytic soot oxidation over the V/MCM-41 catalyst after 54 min of reaction was 0.56 g·kWh⁻¹, which was higher than that of Liu et al., as they reported an energy efficiency of 0.22 g·kWh⁻¹ after 60 min of reaction over the optimized La_{0.5}Ag_{0.5}Mn_{0.8}Co_{0.2}O_{3-δ} catalyst at a discharge power of 10 W and a reaction temperature of 200 °C [12]. In our previous work, the energy efficiency of plasma-catalytic soot oxidation over a V/KIT-6 catalyst was 0.95 g·kWh⁻¹. The improved energy efficiency could be attributed to the strong pore systems of the KIT-6 support, which could facilitate the transportation of O· radicals, O₃ and NO_x within the catalyst layer and accelerate the reaction [38].

2.4. Effect of Operating Parameters

Figure 6 shows the effect of the discharge power on the plasma-catalytic soot oxidation rate and CO₂ selectivity at 30th min over the V/MCM-41 and V/5A catalysts. The soot oxidation rate increases monotonically with increasing discharge power over both the V/MCM-41 and V/5A catalysts. The plasma-catalytic soot oxidation rate over the V/MCM-41 catalyst increases from 73.7% to 94.6% in the discharge power range between 16 W and 24 W, while the value is between 42.3% and 53.9% for the V/5A-packed reactor in the same discharge power range. It is generally recognized that the energetic electrons generated in the micro-discharge streamers are the driving force of plasma-induced reactions because the effective collisions between energetic electrons and carrier gas molecules could facilitate the generation of chemically reactive species, including O, O₃, excited N species, etc. [39]. These species could further react with soot particles and form the final products of CO and CO₂. At a higher discharge power, the generation of more electrons and reactive species could be expected, which would accelerate soot oxidation and improve the oxidation rate of the plasma-catalytic process. Figure 7 also shows the effect of discharge power on the CO₂ selectivity of the plasma-catalytic process over the V/MCM-41 and V/5A catalysts. The CO₂ selectivity decreases with increasing discharge power, while the values for the V/MCM-41 and V/5A catalysts decrease from 52.7% to 47.5% and from 56.9% to 54.2%, respectively. Although more soot particles could be oxidized at a higher discharge power, the slight decrease in CO₂ selectivity at higher discharge powers could also be attributed to the promotion of soot oxidation towards CO rather than the direct oxidation of soot to CO₂ and the oxidation of CO to CO₂, considering the higher activation energy of soot oxidation towards CO compared with the other reaction pathways.

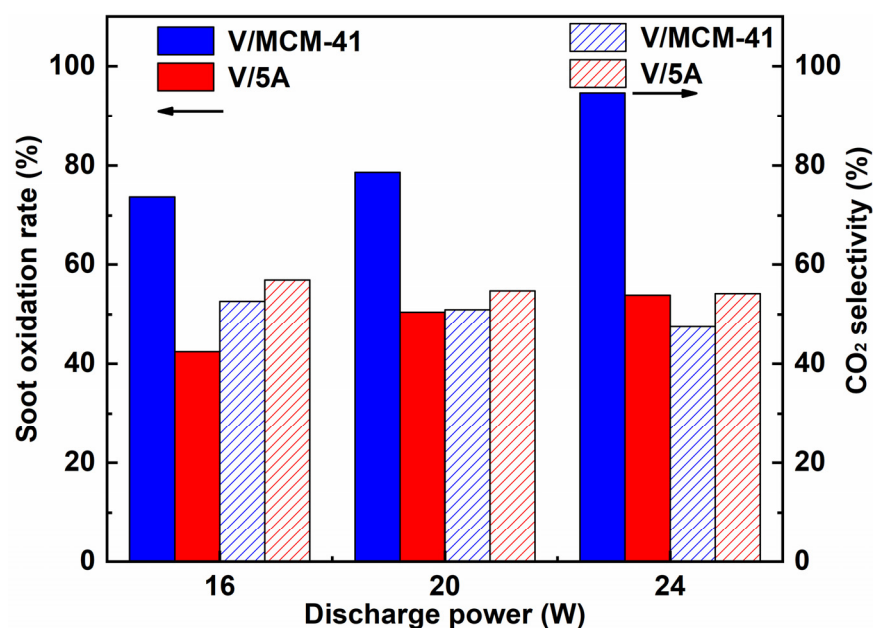


Figure 6. Effect of discharge power on soot oxidation rate and CO₂ selectivity of plasma-catalytic soot oxidation at 30th min over V/MCM-41 and V/5A catalysts (Gas flow rate: 500 mL·min⁻¹ and reaction temperature: 25 °C).

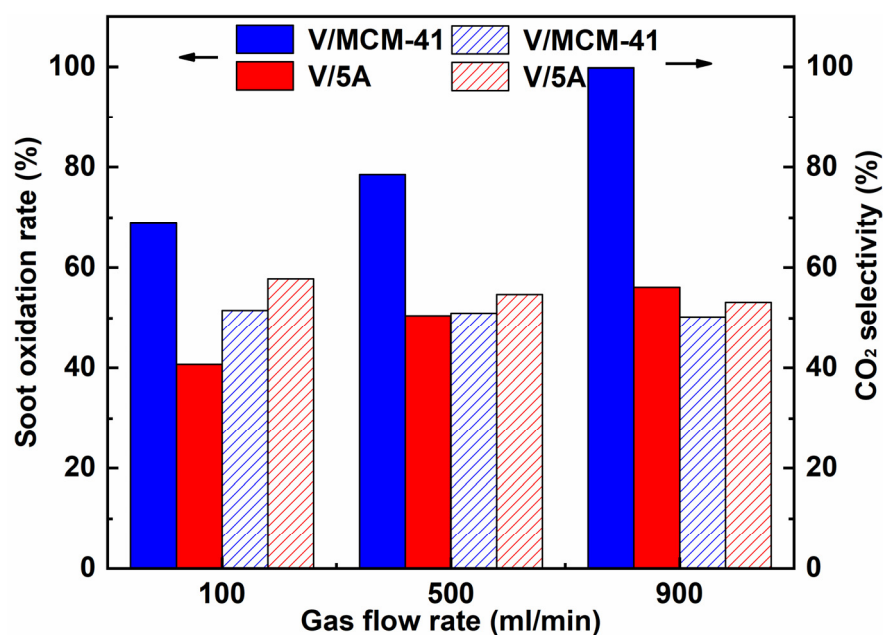


Figure 7. Effect of gas flow rate on soot oxidation rate and CO₂ selectivity of plasma-catalytic soot oxidation at 30th min over V/MCM-41 and V/5A catalysts (Discharge power: 20 W and reaction temperature: 25 °C).

Figure 7 shows the effect of the gas flow rate on plasma-catalytic soot oxidation at the 30th min of the reaction over the V/MCM-41 and V/5A catalysts. In the case of V/MCM-41 catalyst, when the total gas flow rate increases from 100 mL·min⁻¹ to 900 mL·min⁻¹, the soot oxidation rate increases from 68.8% to 99.8%, yet the CO₂ selectivity decreases from 51.6% and 50.2%. On the other hand, the soot oxidation rate increases from 40.7% to 56.1%, yet the CO₂ selectivity decreases from 57.8% and 53.2% within the same range of gas flow rates. The results show that a higher gas flow rate is beneficial for the process of soot oxidation, while the CO₂ selectivity of the process is slightly inhibited. At a high

gas flow rate, more gas molecules would flow through the discharge region during the reaction process. Due to the decreased residence time of molecules in the carrier gas, the concentration of reactive species like $O\cdot$ radicals and O_3 would decrease in the effluent. However, the total amount of plasma-generated reactive species generated inside the plasma region within the reaction period would increase, considering the increase in the gas flow rate [40]. As a result, more reactive species could be used in the soot oxidation process, which accelerates the reaction and leads to improvements in the soot oxidation rate at higher gas flow rates [19]. On the other hand, since the activation energy barrier of CO oxidation to CO_2 is much higher than that of soot oxidation to CO, it is reasonable to deduce that most of the reactive species would participate in the oxidation of soot to CO rather than soot to CO_2 . Consequently, the CO_2 selectivity of the process would decrease due to the formation of more CO at high gas flow rates.

The effect of reaction temperature on plasma-catalytic soot oxidation at the 30th min of the reaction over the V/MCM-41 and V/5A catalysts is presented in Figure 8. For both cases, the soot oxidation rate decreases with increasing temperature. For the V/MCM-41 catalyst, the oxidation rate decreases from 78.6% at 25 °C to 71.3% at 150 °C, while the value for the V/5A catalyst decreases from 50.4% to 44.5% in the same temperature range. On the contrary, the CO_2 selectivity remains almost constant: the values are in the range of 51.0% to 51.7% for the V/MCM-41 catalyst and 53.9% to 54.8% for the V/5A catalyst. As discussed above, the plasma-generated reactive species played a vital role in the plasma-catalytic soot oxidation process. However, based on the theory of chemical reaction kinetics, an increase in reaction temperature could enhance the Brownian motion of these reactive species, which would increase the possibilities of effective collisions between these reactive species and other gaseous molecules (e.g., N_2 , O_2 , etc.) [31]. For example, the lifetime of an O_3 molecule at room temperature (~ 25 °C) could be over 30 min, but the value could be less than 1 s at 150 °C to 300 °C [41]. As a result, most of the reactive species generated in the gas phase of the plasma region may not be able to reach the interfaces of “catalyst-soot” and “gas-soot”. Thus, the possibilities of effective utilization of these reactive species would be reduced, leading to a decrease in the soot oxidation rate. It can be deduced that increasing the reaction temperature would not significantly affect the reaction pathways of CO_2 formation in the plasma-catalytic soot oxidation system, and similar results have been widely reported in plasma-induced oxidation processes [11,42].

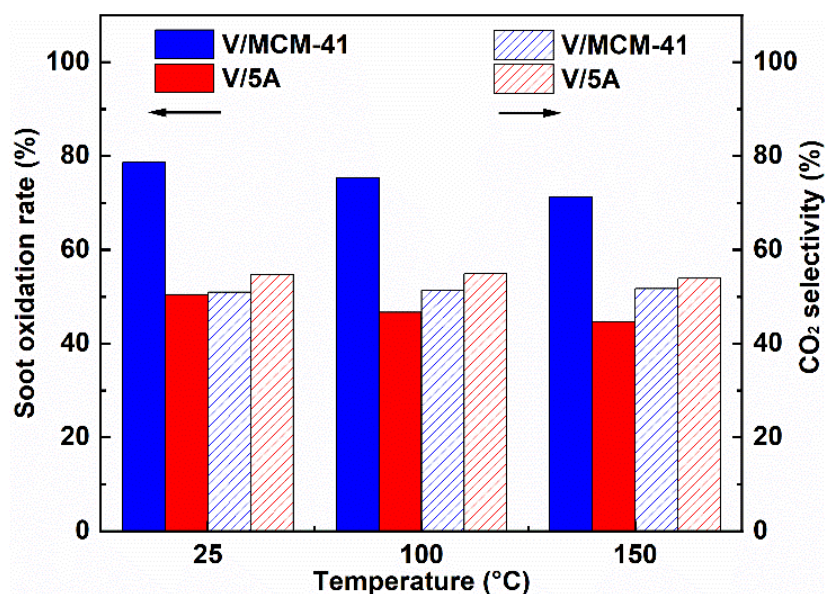


Figure 8. Effect of reaction temperature on soot oxidation rate and CO_2 selectivity of plasma-catalytic soot oxidation at 30th min over V/MCM-41 and V/5A catalysts (Discharge power: 20 W and gas flow rate: $500\text{ mL}\cdot\text{min}^{-1}$).

3. Materials and Methods

3.1. Catalyst Preparations

In this work, the V/M (M = MCM-41, mordenite, USY and 5A) catalysts were prepared using the wet impregnation method. The catalyst precursors used in this work, including ammonium metavanadate, oxalic acid and zeolites, were of analytical grade and purchased from Macklin Co., Ltd. (Shanghai, China). The physical properties of the zeolite supports are listed in Table S1. Firstly, weighted amount of ammonium metavanadate (0.1146 g) and oxalic acid (0.2471 g) were dissolved in 30 mL deionized water and steadily stirred at room temperature for 2 h; the molar ratio of the two chemicals was 1:2. A calculated amount of the zeolite support (4.95 g) was then added to the obtained solution, which was then magnetically stirred for 4 h at 80 °C. The resulting paste was dried at 110 °C in an oven for 12 h, then calcined in a muffle at 500 °C for 5 h. All of the catalysts were sieved using 40–60 meshes prior to use. The prepared catalysts were denoted as V/M, where M was the zeolite type of the support. The loading amount of vanadium species was 1 wt.% in this work.

3.2. Catalyst Characterizations

The N₂ adsorption–desorption experiments were performed at −77 °C using a Quantachrome Autosorb-1 system. The catalysts were degassed at 250 °C for 3 h to purify any impurities before the test. The values of specific surface area (S_{BET}) were calculated using the Brunauer–Emmett–Teller (BET) equation.

X-ray powder diffraction (XRD) analysis was performed using a Rikagu D/max-2000 X-ray diffractometer with Cu-K α radiation. The scanning range was between 20° and 80°, while the scanning rate was 2°·min^{−1} with a step size of 0.02°. The crystalline size calculation was conducted using Scherrer's equation.

X-ray photoelectron spectroscopy (XPS) was conducted with a Thermo ESCALAB 250 electron spectrometer using an Al K α X-ray source ($h\nu = 1486.6$ eV) at 150 W. The binding energy was calibrated to the C 1s spectra at the binding energy (B.E.) value of 284.8 eV from adventitious carbon.

Temperature-programmed reduction of H₂ (H₂-TPR) and temperature-programmed desorption of O₂ (O₂-TPD) were performed on a Micromeritics ChemiSorb 2720 instrument. In each test of H₂-TPR, 100 mg catalysts were firstly heated at 250 °C in a flowing helium gas stream (30 mL·min^{−1}) for 1 h and then cooled to room temperature. The carrier gas was then switched to a 5 vol.% H₂/Ar mixture with the same gas flow rate. The temperature was then increased from 50 °C to 800 °C at a heating rate of 10 °C·min^{−1}. The H₂ consumption amount was recorded continuously. Similarly, for the O₂-TPD test, 100 mg catalysts were heated at 250 °C in a flowing helium gas stream (30 mL·min^{−1}) for 1 h and then cooled to room temperature. The sample was then treated in a 3 vol.% O₂/He mixture at 30 mL·min^{−1} for 1 h at room temperature. The sample was consequently purged in pure helium gas flow for 1 h to remove the impurities. Finally, the temperature was then increased to 800 °C at a heating rate of 10 °C·min^{−1}. The amount of O₂ desorption was then recorded.

3.3. Plasma-Catalytic System

Figure 9 shows the experimental diagram of the plasma-catalytic system. Here, gas cylinders (with a purity of 99.99%) were purchased from Fangxin, Ningbo, China and used to generate the carrier gas (10 vol.% O₂ with balanced N₂). The two gas streams of O₂ and N₂ were regulated by mass flow controllers (Sevenstars D07-B, Beijing, China). The gas streams were mixed before being introduced to the reactor. The total gas flow rate was 500 mL·min^{−1} unless otherwise specified.

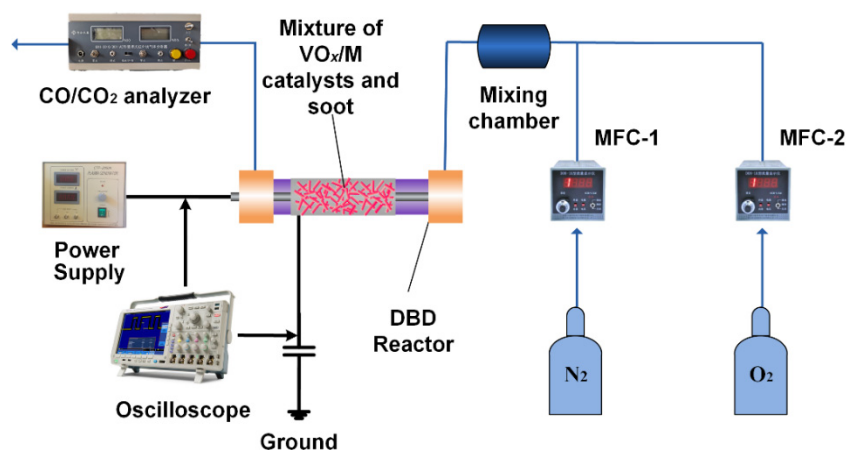


Figure 9. Experimental system for plasma-catalytic soot oxidation.

The reactor consisted of a quartz tube with an outer diameter of 10 mm and an inner diameter of 8 mm. A stainless-steel rod with a diameter of 4 mm was fixed on the axis of the quartz tube as a high-voltage electrode, while the ground electrode was a stainless-steel mesh wrapping around the quartz tube. The soot (160–200 meshes, Printex-U from Degussa) particles were mixed with the catalyst using a spatula. The weight ratio of soot to catalyst was 1:9 under loose contact mode. For each test, 100 mg mixtures of soot and V/M catalyst were packed into the discharge region and held by quartz wool.

The reactor was powered by an AC high-voltage power supply (CTP-2000K, Nanjing Suman, China). The applied voltages of the plasma reactor and the voltage across the external measuring capacitor C_{ext} (0.47 μF) were measured using a Testec voltage probe (HVP-15HF, 1000:1) and a Tektronix P5100 probe, respectively. The voltage signals were recorded using a Tektronix 2014B oscilloscope, while the Q-U Lissajous method was used to calculate the discharge power. The whole process of plasma-catalytic soot oxidation was performed for 60 min unless otherwise specified. In addition, the reactor was placed in a specially designed and well-grounded oven to evaluate the effect of heating temperature on the process of plasma-catalytic soot oxidation at a fixed heating temperature and discharge power. The heating temperature could be adjusted from room temperature to 200 $^{\circ}\text{C}$ with an accuracy of ± 1 $^{\circ}\text{C}$.

The discharge power of the DBD can be calculated by the following method:

$$P(W) = f \times C_m \times A \quad (8)$$

where f , C_m and A are the discharge frequency (10.1 kHz), the measuring capacitance (0.47 μF) and the area of the Lissajous figure, respectively.

The concentrations of CO and CO₂ were measured using an online infrared gas analyzer (GXH-3010/3011AE, Huayun, China) with an accuracy of $\pm 3\%$. The soot oxidation rate (X_{soot}) and CO₂ selectivity of the process were calculated as follows:

$$X_{soot}(\%) = \frac{\int_0^t (c_{CO} + c_{CO_2}) dt}{m_{soot}} \times 100\% \quad (9)$$

$$\text{CO}_2\text{selectivity}(\%) = \frac{\int_0^t c_{CO_2} dt}{\int_0^t (c_{CO} + c_{CO_2}) dt} \times 100\% \quad (10)$$

where C_{CO} and C_{CO_2} are the outlet concentrations of CO and CO₂, respectively; m_{soot} is the weight of initially packed soot for each test.

4. Conclusions

In this work, plasma-catalytic soot oxidation was performed over a series V/M catalysts using MCM-41, mordenite, USY and 5A as supports. The soot oxidation rate followed an order of V/MCM-41 > V/mordenite > V/USY > V/5A, while the CO₂ selectivity of the process followed the opposite order of the oxidation rate over the V/M catalysts. A wide range of catalyst characterizations, including N₂ adsorption–desorption, XRD, XPS and H₂-TPR, were performed to obtain insights regarding the reaction mechanisms of soot oxidation in plasma-catalytic systems. The high V⁴⁺/(V⁴⁺ + V⁵⁺) and O_{ads}/(O_{ads} + O_{latt}) values of the V/MCM-41 catalyst indicated abundant oxygen vacancies on its surface, which would contribute to the release of O_{ads} species with better mobility for soot oxidation. The lower reduction temperature of the V/MCM-41 catalyst also confirmed its better reducibility, suggesting the facility of O_{ads} activation over V/MCM-41 packed in the plasma region. These properties of V/M catalysts would benefit soot oxidation. However, due to the properties of soot particles, the oxidation of soot to CO is predominant over direct soot oxidation towards CO₂. Thus, the CO₂ selectivity decreased in the presence of catalysts with higher soot oxidation rates in this work. The effects of discharge power, gas flow rate and reaction temperature on soot oxidation were also investigated. The results showed that higher discharge power, higher gas flow rate and lower reaction temperature were conducive to soot oxidation, while CO₂ selectivity was simultaneously inhibited.

Supplementary Materials: The following supporting information can be downloaded at: <https://www.mdpi.com/article/10.3390/catal12070677/s1>, Table S1: Textural properties of the zeolite support; Figure S1: SEM images of the V/M catalysts: (a,b) V/MCM-41; (c,d) V/Mordenite; (e,f) V/USY; (g,h) V/5A. Left column: with a magnitude of 5.0 k, right column: with a magnitude of 50.0 k; Figure S2: XRD patterns of the zeolite supports; Figure S3: O 1s spectra of all zeolite supports.

Author Contributions: Conceptualization, X.Z., Z.Z. and G.Y.; Data curation, H.W. and J.L. (Jianbin Luo); Formal analysis, X.Z., H.W., J.L. (Jianbin Luo) and Z.Y.; Funding acquisition, X.Z.; Investigation, H.W., J.Y., J.L. (Jianbin Luo) and Y.J.; Methodology, J.L. (Jin Liu), J.Y. and Y.J.; Resources, Z.Z. and G.C.; Writing—original draft, X.Z. and J.L. (Jin Liu); Writing—review and editing, X.Z., Z.Z. and G.C. All authors have read and agreed to the published version of the manuscript.

Funding: This work is funded by the National Natural Science Foundation of China (No.51976093), the K.C. Wong Magna Fund in Ningbo University and Qingdao Science and Technology Demonstration and Guidance Project for Benefiting the People (No. 21-1-4-sf-8-nsh).

Data Availability Statement: The data presented in this study are available on request from the corresponding author.

Acknowledgments: X.Z. would like to thank the support from the National Natural Science Foundation of China (No. 51976093) and the K.C. Wong Magna Fund in Ningbo University. Y.J. and Z.Y. are funded by the Qingdao Science and Technology Demonstration and Guidance Project for Benefiting the People (No. 21-1-4-sf-8-nsh). X.Z. and H.W. would also like to thank the support for catalyst characterization from Suzhou Deyo Bot Advanced Materials Co., Ltd.

Conflicts of Interest: The authors declare no conflict of interest.

References

1. Sawatmongkhon, B.; Theinnoi, K.; Wongchang, T.; Haoharn, C.; Wongkhorsub, C.; Sukjit, E.; Tsolakis, A. Catalytic oxidation of diesel particulate matter by using silver and ceria supported on alumina as the oxidation catalyst. *Appl. Catal. A Gen.* **2019**, *574*, 33–40. [[CrossRef](#)]
2. Ou, J.; Meng, Z.; Hu, Y.; Du, Y. Experimental investigation on the variation characteristics of soot layer thickness and pressure drop during DPF/CDPF active regeneration. *Chem. Eng. Sci.* **2021**, *241*, 116682. [[CrossRef](#)]
3. Liang, X.; Lv, X.; Wang, Y.; He, L.; Wang, Y.; Fu, K.; Liu, Q.; Wang, K. Experimental investigation of diesel soot oxidation reactivity along the exhaust after-treatment system components. *Fuel* **2021**, *302*, 121047. [[CrossRef](#)]
4. Mishra, A.; Prasad, R. Preparation and application of perovskite catalysts for diesel soot emissions control: An overview. *Catal. Rev.* **2014**, *56*, 57–81. [[CrossRef](#)]
5. Dhal, G.C.; Mohan, D.; Prasad, R. Preparation and application of effective different catalysts for simultaneous control of diesel soot and nox emissions: An overview. *Catal. Sci. Technol.* **2017**, *7*, 1803–1825. [[CrossRef](#)]

6. Liu, J.; Yang, J.; Sun, P.; Ji, Q.; Meng, J.; Wang, P. Experimental investigation of in-cylinder soot distribution and exhaust particle oxidation characteristics of a diesel engine with nano-CeO₂ catalytic fuel. *Energy* **2018**, *161*, 17–27. [[CrossRef](#)]
7. Mori, K.; Miyauchi, Y.; Kuwahara, Y.; Yamashita, H. Shape effect of MnO_x-decorated CeO₂ catalyst in diesel soot oxidation. *Bull. Chem. Soc. Jpn.* **2017**, *90*, 556–564. [[CrossRef](#)]
8. Shareei, M.; Taghvaei, H.; Azimi, A.; Shahbazi, A.; Mirzaei, M. Catalytic dbd plasma reactor for low temperature partial oxidation of methane: Maximization of synthesis gas and minimization of CO₂. *Int. J. Hydrogen Energy* **2019**, *44*, 31873–31883. [[CrossRef](#)]
9. Zhang, Z.; Jiang, Z.; Shangguan, W. Low-temperature catalysis for VOCs removal in technology and application: A state-of-the-art review. *Catal. Today* **2016**, *264*, 270–278. [[CrossRef](#)]
10. Zheng, Y.; Grant, R.; Hu, W.; Marek, E.; Scott, S.A. H₂ production from partial oxidation of CH₄ by Fe₂O₃-supported Ni-based catalysts in a plasma-assisted packed bed reactor. *Proc. Combust. Inst.* **2019**, *37*, 5481–5488. [[CrossRef](#)]
11. Lu, H.; Yao, X.; Li, J.; Yao, S.; Wu, Z.; Zhang, H.; Lin, H.; Nozaki, T. Mechanism on the plasma-catalytic oxidation of graphitic carbon over Au/γ-Al₂O₃ by in situ plasma drifts-mass spectrometer. *J. Hazard. Mater.* **2020**, *396*, 122730. [[CrossRef](#)] [[PubMed](#)]
12. Liu, S.; Liu, Y.; Tang, D.; Miao, Y.; Cao, Z.; Zhao, Z. Synergy of NTP-La_{1-x}Ag_xMn_{1-y}Co_yO_{3-δ} hybrid for soot catalytic combustion at low temperature. *Plasma Chem. Plasma Process.* **2021**, *41*, 1009–1019. [[CrossRef](#)]
13. Whitehead, J.C. Plasma-catalysis: The known knowns, the known unknowns and the unknown unknowns. *J. Phys. D Appl. Phys.* **2016**, *49*, 243001. [[CrossRef](#)]
14. Bogaerts, A.; Tu, X.; Whitehead, J.C.; Centi, G.; Lefferts, L.; Guaitella, O.; Azzolina-Jury, F.; Kim, H.-H.; Murphy, A.B.; Schneider, W.F.; et al. The 2020 plasma catalysis roadmap. *J. Phys. D Appl. Phys.* **2020**, *53*, 443001. [[CrossRef](#)]
15. Patil, B.S.; Cherkasov, N.; Srinath, N.V.; Lang, J.; Ibadon, A.O.; Wang, Q.; Hessel, V. The role of heterogeneous catalysts in the plasma-catalytic ammonia synthesis. *Catal. Today* **2021**, *362*, 2–10. [[CrossRef](#)]
16. Kim, H.H.; Teramoto, Y.; Sano, T.; Negishi, N.; Ogata, A. Effects of Si/Al ratio on the interaction of nonthermal plasma and ag/hy catalysts. *Appl. Catal. B: Environ.* **2015**, *166*, 9–17. [[CrossRef](#)]
17. Xie, D.Y.; Sun, Y.; Zhu, T.L.; Hou, L.Y.; Hong, X.W. Nitric oxide oxidation and its removal in mist by nonthermal plasma: Effects of discharge conditions. *Ind. Eng. Chem. Res.* **2017**, *56*, 11336–11343. [[CrossRef](#)]
18. Shi, Y.; Cai, Y.; Fan, R.; Cui, Y.; Chen, Y.; Ji, L. Characterization of soot inside a diesel particulate filter during a nonthermal plasma promoted regeneration step. *Appl. Therm. Eng.* **2019**, *150*, 612–619. [[CrossRef](#)]
19. Pu, X.; Cai, Y.; Shi, Y.; Wang, J.; Gu, L.; Tian, J.; Li, W. Diesel particulate filter (DPF) regeneration using non-thermal plasma induced by dielectric barrier discharge. *J. Energy Inst.* **2018**, *91*, 655–667. [[CrossRef](#)]
20. Ji, P.; Gao, X.; Du, X.; Zheng, C.; Luo, Z.; Cen, K. Relationship between the molecular structure of V₂O₅/TiO₂ catalysts and the reactivity of SO₂ oxidation. *Catal. Sci. Technol.* **2016**, *6*, 1187–1194. [[CrossRef](#)]
21. Zhu, X.; Gao, X.; Yu, X.; Zheng, C.; Tu, X. Catalyst screening for acetone removal in a single-stage plasma-catalysis system. *Catal. Today* **2015**, *256*, 108–114. [[CrossRef](#)]
22. Wei, L.; Kumar, N.; Haije, W.; Peltonen, J.; Peurla, M.; Grénman, H.; de Jong, W. Can bi-functional nickel modified 13X and 5A zeolite catalysts for CO₂ methanation be improved by introducing ruthenium? *Mol. Catal.* **2020**, *494*, 111115. [[CrossRef](#)]
23. Einaga, H.; Teraoka, Y.; Ogata, A. Catalytic oxidation of benzene by ozone over manganese oxides supported on usy zeolite. *J. Catal.* **2013**, *305*, 227–237. [[CrossRef](#)]
24. de Oliveira, A.M.; Crizel, L.E.; da Silveira, R.S.; Pergher, S.B.C.; Baibich, I.M. NO decomposition on mordenite-supported pd and cu catalysts. *Catal. Commun.* **2007**, *8*, 1293–1297. [[CrossRef](#)]
25. Liu, L.; Shen, B.; Si, M.; Yuan, P.; Lu, F.; Gao, H.; Yao, Y.; Liang, C.; Xu, H. Mn-based catalysts supported on γ-Al₂O₃, TiO₂ and MCM-41: A comparison for low-temperature no oxidation with low ratio of O₃/NO. *RSC Adv.* **2021**, *11*, 18945–18959. [[CrossRef](#)] [[PubMed](#)]
26. Wu, J.; Zhu, X.; Cai, Y.; Tu, X.; Gao, X. Coupling nonthermal plasma with V₂O₅/TiO₂ nanofiber catalysts for enhanced oxidation of ethyl acetate. *Ind. Eng. Chem. Res.* **2019**, *58*, 2–10. [[CrossRef](#)]
27. He, F.; Luo, J.; Liu, S. Novel metal loaded KIT-6 catalysts and their applications in the catalytic combustion of chlorobenzene. *Chem. Eng. J.* **2016**, *294*, 362–370. [[CrossRef](#)]
28. Yao, X.; Zhang, J.; Liang, X.; Long, C. Plasma-catalytic removal of toluene over the supported manganese oxides in DBD reactor: Effect of the structure of zeolites support. *Chemosphere* **2018**, *208*, 922–930. [[CrossRef](#)] [[PubMed](#)]
29. Jiang, N.; Zhao, Y.; Qiu, C.; Shang, K.; Lu, N.; Li, J.; Wu, Y.; Zhang, Y. Enhanced catalytic performance of CoO_x-CeO₂ for synergetic degradation of toluene in multistage sliding plasma system through response surface methodology (RSM). *Appl. Catal. B Environ.* **2019**, *259*, 118061. [[CrossRef](#)]
30. Nagle, J. Oxidation of carbon between 1000–2000 °C. In Proceedings of the Fifth Conference on Carbon, London, UK, 1962.
31. Turns, S.R. *An Introduction to Combustion: Concepts and Applications*, 2nd ed.; McGraw-Hill Education: New York, NY, USA, 1985.
32. Li, Z.; Zhang, W.; Chen, Z.; Jiang, Q. Mechanism of accelerating soot oxidation by NO₂ from diesel engine exhaust. *Environ. Pollut.* **2020**, *264*, 114708. [[CrossRef](#)] [[PubMed](#)]
33. Liu, J.; Zhu, X.; Hu, X.; Zhang, F.; Tu, X. Plasma-assisted ammonia synthesis in a packed-bed dielectric barrier discharge reactor: Effect of argon addition. *Vacuum* **2022**, *197*, 110786. [[CrossRef](#)]
34. Roland, U.; Holzer, F.; Poppl, A.; Kopinke, F.D. Combination of non-thermal plasma and heterogeneous catalysis for oxidation of volatile organic compounds part 3. Electron paramagnetic resonance (EPR) studies of plasma-treated porous alumina. *Appl. Catal. B: Environ.* **2005**, *58*, 227–234. [[CrossRef](#)]

35. Zheng, L.; Zimina, A.; Casapu, M.; Grunwaldt, J.D. Hydrocarbon and soot oxidation over cerium and iron doped vanadium SCR catalysts. *ChemCatChem* **2020**, *12*, 6272–6284. [[CrossRef](#)]
36. Zhu, X.; Zhang, S.; Yang, Y.; Zheng, C.; Zhou, J.; Gao, X.; Tu, X. Enhanced performance for plasma-catalytic oxidation of ethyl acetate over $\text{La}_{1-x}\text{Ce}_x\text{CoO}_{3+\delta}$ catalysts. *Appl. Catal. B-Environ.* **2017**, *213*, 97–105. [[CrossRef](#)]
37. Ranji-Burachaloo, H.; Masoomi-Godarzi, S.; Khodadadi, A.A.; Mortazavi, Y. Synergetic effects of plasma and metal oxide catalysts on diesel soot oxidation. *Appl. Catal. B: Environ.* **2016**, *182*, 74–84. [[CrossRef](#)]
38. Wu, H.; Zhu, X.; Wu, X.; Tu, X.; Chen, G.; Yang, G. Plasma-catalytic reactions for soot oxidation on VO_x/M (M = KIT-6, SBA-15 and SiO_2) catalysts: Influence of pore structure. *ChemistrySelect* **2022**, *7*, e202103545. [[CrossRef](#)]
39. Chang, T.; Ma, C.; Shen, Z.; Veerapandian, S.K.P.; Huang, Y.; De Geyter, N.; Morent, R. Mn-based catalysts for post non-thermal plasma catalytic abatement of vocs: A review on experiments, simulations and modeling. *Plasma Chem. Plasma Process.* **2021**, *41*, 1239–1278. [[CrossRef](#)]
40. Országh, J.; Skalný, J.D.; Mason, N.J. Ozone formation in a coaxial DC corona discharge under carbon dioxide gas flow. *Plasma Process. Polym.* **2007**, *4*, 694–700. [[CrossRef](#)]
41. Zhu, X.; Gao, X.; Zheng, C.; Wang, Z.; Ni, M.; Tu, X. Plasma-catalytic removal of a low concentration of acetone in humid conditions. *RSC Adv.* **2014**, *4*, 37796–37805. [[CrossRef](#)]
42. Yao, S.L.; Shen, X.; Zhang, X.M.; Han, J.Y.; Wu, Z.L.; Tang, X.J.; Lu, H.; Jiang, B.Q. Sustainable removal of particulate matter from diesel engine exhaust at low temperature using a plasma-catalytic method. *Chem. Eng. J.* **2017**, *327*, 343–350. [[CrossRef](#)]